JMEPEG (2019) 28:5702–5715
https://doi.org/10.1007/s11665-019-04315-5

1059-9495/$19.00

Mg-3Zn/HA Biodegradable Composites Synthesized via Spark Plasma Sintering for Temporary Orthopedic Implants

Anshu Dubey, Satish Jaiswal, Swati Haldar, Partha Roy, and Debrupa Lahiri

(Submitted March 14, 2019; in revised form July 25, 2019; published online September 10, 2019)

In the present study, an attempt has been made to improve the mechanical properties, biocompatibility and degradation rate of Mg/3Zn matrix composite, by reinforcing with chemically inert and osteoconductive hydroxyapatite (HA). The composites were synthesized through spark plasma sintering for better consolidation. The HA content, in Mg/3Zn matrix, was optimized with an aim of improving mechanical behavior, corrosion resistance and biocompatibility simultaneously. It has been observed that reinforcement with 15 wt.% HA could slow down the corrosion rate by ~ 60% and improve the hardness and compression strength by ~ 42.8 and 18%, respectively. In vitro studies, up to 56 days, unveil the effect of HA reinforcement in corrosion resistance of magnesium-based matrix. Osteoblastic activity has shown better cell proliferation on the composite surfaces, which were reinforced with HA.

Keywords biodegradable, hydroxyapatite, in vitro corrosion, magnesium, orthopedic applications, spark plasma sintering

1. Introduction

Adequate selection of orthopedic implants is a key factor for better and long-term success of implants (Ref 1). Different metallic materials, e.g., titanium alloys, cobalt chromium alloys and stainless steel, have been in use for orthopedic applications, due to their excellent mechanical properties, good corrosion resistance and reasonable biocompatibility. However, stress shielding effect, caused by their high elastic modulus, in comparison with natural bone, and non-biodegradability in physiological environment are the major limitations of these metallic materials in temporary implant applications (Ref 2-6). In this connection, the demand of biodegradable material has globally risen. Magnesium (Mg) has shown a great potential as a biocompatible metal with similar mechanical properties, i.e., elastic modulus to that of human bone, which can overcome stress shielding effect. Furthermore, it has ability for in vivo degradation (Ref 7-9). Nevertheless, rapid degradation of Mg, in vivo, is a major challenge (Ref 10). It is also associated with the early deterioration of mechanical properties in vivo. Thus, the prime objective was to reduce the degradation rate; the viable solutions available for the same are surface modification and fabrication of composites (Ref 11).

The benefits of using metal matrix composites as biodegradable materials are their adjustable mechanical properties (elastic modulus, compressive strength). In addition to that, corrosion properties can also be tailored by choosing the optimized composition of reinforcement (Ref 12, 13). An appropriate method to tailor corrosion of Mg is to increase the surrounding pH to stabilize the degradation products in the protective corrosion layer. In connection to this, particularly Ca is known to reduce the vulnerability of Mg to degrade, when added in lower content (< 1.3 wt.%) (Ref 14). Various reinforcement [i.e., calcium phosphate-based ceramic (Ref 15-18), bioactive glass (Ref 19), zinc oxide (Ref 20) and calcium particles (Ref 21)], with different size, content and distribution, has been employed to tailor the corrosion resistance of magnesium. Hydroxyapatite (HA), a naturally existing element form of calcium phosphate hydroxide, with the chemical formula $Ca_5(PO4)_3(OH)$, is also known to have a less solubility in biological environment (Ref 22) and possesses excellent biocompatibility and bioactivity. These are attributed to its structural and chemical similarities to the human bone composition (Ref 23). The bioactive nature of HA promotes cell viability and thus ability to promote new bone growth on implants. Mg-based composites reinforced with 1 wt.% nano-HA offers better mineralization of apatite, while exposed to concentrated simulated body fluid (SBF) (Ref 24). Hence, HA is accepted to be a potential mineral as the reinforcement for the synthesis of Mg alloys/HA composites. In connection to this, Witte et al. (Ref 14) fabricated the AZ91D/HA (20 wt.%) MMCs by powder processing method and observed that it was biodegradable, with ~ 37% improvement in degradation resistance, as compared to that of bare AZ91D alloy. However,

Anshu Dubey and **Satish Jaiswal**, Biomaterials and Multiscale Mechanics Laboratory, Department of Metallurgical and Materials Engineering, Indian Institute of Technology Roorkee, Roorkee, Uttarakhand 247667, India; **Swati Haldar**, Centre for Nanotechnology, Indian Institute of Technology Roorkee, Roorkee, Uttarakhand 247667, India; and **Partha Roy**, Centre for Nanotechnology, Indian Institute of Technology Roorkee, Roorkee, Uttarakhand 247667, India; and Department of Biotechnology, Indian Institute of Technology Roorkee, Roorkee, Uttarakhand 247667, India; **Debrupa Lahiri**, Biomaterials and Multiscale Mechanics Laboratory, Department of Metallurgical and Materials Engineering, Indian Institute of Technology Roorkee, Roorkee, Uttarakhand 247667, India; and Centre for Nanotechnology, Indian Institute of Technology Roorkee, Roorkee, Uttarakhand 247667, India. Contact e-mail: dlahifmt@iitr.ac.in.

a concern about biocompatibility is associated with this alloy due to the presence of Al as alloying element, which is known as a neurotoxicant and closely related to numerous neurological disorders, such as Alzheimer disease, dementia and senile dementia (Ref 25). Thus, this system might not be appropriate matrix of biomaterial composites. In another study, Mg-3Zn alloy is reinforced with HA through selective laser melting, which leads to the slowdown of degradation rate due to formation of apatite layer on the surface (Ref 26). Ye et al. have also reported the capability of Mg-3Zn-0.5Zr matrix with various content of HA (0.5, 1 and 1.5 wt.%) to tailor the mechanical and degradation behavior of composite. HA reinforcement of 1.5 wt.% was found to enhance the yield strength, ultimate tensile strength (UTS) and elongation by 16,10 and 46%, respectively (Ref 27). However, the UTS of Mg-3Zn-0.5Zr/1.5HA composite is 302 MPa, which is way higher than that of cortical bone (Ref 28). It might cause the probability of aseptic loosening further effect of stress shielding. Additionally, bioactive nature of alloys of Zr is yet not confirmed. High concentration of Zr in liver makes it more acidic (Ref 8). Another research group synthesized Mg-3Zn-0.2Ca/1HA (wt.%) composite through high shear solidification (HSS) and hot extrusion route. The ultimate tensile strength and elongation of the extruded composite were 322 MPa, 341 MPa and 7.6%, respectively, which are much higher as compared to natural bone. Apparently, the degradation rate of the as-extruded Mg-3Zn-0.2Ca/1HA composite was measured to be 1.52 mm/y. However, long-term immersion studies were not reported (Ref 29). Addition of calcium will form intermetallic which are harmful for human body. Campo et al. (Ref 30) reported Mg/HA composite, synthesized by powder metallurgy, with $\sim$ 65% enhancement in degradation rate. However, incorporation of 15 wt.% HA to Mg resulted in decrement in compressive yield strength by $\sim$ 5%. Contradictory to this, Khanra et al. (Ref 22) synthesized Mg-15 wt.% HA composite by liquid processing route and observed 15% improvement in compressive yield strength. However, no evaluation of degradation was reported by the authors, which is required to evaluate the clinical acceptability. In connection to this, Jaiswal et al. (Ref 31) fabricated Mg-3Zn/HA composite by powder processing route, using conventional sintering process and found that addition of 5 wt.% HA could improve corrosion resistance of Mg-3Zn by 42% and compressive yield strength by 23%. Hence, it is noted that mechanical behavior of composites is greatly influenced by processing method. Powder processing route can become an even more effective synthesis method, if sintering can be completed in a very short duration and introducing no impurity, defects and minimal porosity in the structure. Spark plasma sintering (SPS) is one of such consolidation processes, which can fulfill these requirements.

Pulse electric current sintering (PECS), also known as spark plasma sintering (SPS), is a relatively a new technique, which can remarkably enhance the quality of sintered specimen. SPS consolidation provides significant advantages, by both lowering the required sintering temperature and shortening its duration, resulting in high-quality densification. It utilizes release of electrical energy via arcing at the porous regions between powders to create local plasma and allows enhanced mass transport in the neck region to achieve full densification.

Researchers have fabricated magnesium matrix composites with different HA wt.% (0, 8, 10 and 15 wt.%) through ball milling following the by SPS (Ref 32). There was remarkable improvement in corrosion resistance by $\sim$ 98.7% and $\sim$ 4% improvement in fracture toughness by incorporation of 10 wt.% HA in Mg/HA composite. However, there was no report on biocompatibility and in vitro degradability. One recent report has shown the effect of nano-HA on the mechanical degradation and biocompatibility of Mg-Zn/HA composite through spark plasma sintering (Ref 33). They have reported improvement in compressive and bending strength by 43% and 14%, respectively. Furthermore, the corrosion resistance was reported to improve by 49%. The cytotoxicity test revealed biocompatible behavior of Mg-Zn/HA composites. Nevertheless, the study claimed the use of 5.5 wt.% of Zn with magnesium, which is not desirable quantity according to the previous literature (Ref 6, 11). Also, no study was performed on the long duration of immersion of magnesium in any physiological environment (Ref 33).

Though there are reports on Mg/HA composites for orthopedic application, the previous studies did not establish an optimized composition, mechanically, degradation-wise and biologically suitable for orthopedic application. There is no significant study on microstructure, mechanical properties, degradation rate in long-term exposure of samples in SBF, accelerated corrosion rate and biocompatibility to assess cell viability of Mg-3Zn-based composites, with HA reinforcement and synthesized by SPS technology. This is required to establish clinical use of Mg-based totally biodegradable temporary orthopedic implants/accessories.

In context of the above scenario, the main aim of this study is to synthesize magnesium-based metal matrix composite (MMC) with various content of HA as a reinforcement and to get an idea of this composite in connection with corrosion, biocompatibility and mechanical properties for fracture fixing accessories application. This research demonstrates the synthesis of Mg-3Zn/HA composite, aimed for fracture fixing accessories, by sonication and subsequent SPS and analyzing the effect of HA as reinforcement on Mg-3Zn matrix. The microstructure and degradation behaviors of Mg-3Zn/HA composites, in simulated body fluid, are studied with the help of optical microscopy, x-ray diffraction and potentiodynamic polarization test. The degradation behavior of material system, as a function of mass loss in simulated body fluid, is evaluated to assess the performance of this material system in simulated service condition. Cytocompatibility of these composite structures was evaluated, in terms of adhesion and proliferation of bone-forming cells on their surface by in vitro studies. All these data helped in understanding the potential of this material system in temporary orthopedic implant application.

2. Materials and Methods

2.1 Fabrication of Composites

In the current study, Mg-3Zn/HA composite with varying content of HA (0, 5, 10, 15 and 20 wt.%) was synthesized through powder metallurgy route via spark plasma sintering technique. Magnesium powder (purity $>$ 99%, density 1.71 g/cm^3), with an average particle size of 130 $\pm$ 15 μm, was acquired from CMERI CSIR, Durgapur. Zinc powder (purity $>$ 99.8%, density 6.61 g/cm^3), with particle size of 30 $\pm$ 5 μm, was purchased from Shubhmets, Mumbai. Nano-hydroxyapatite powder has cylindrical shape, which has an average height 180 $\pm$ 20 nm and diameter 83 $\pm$ 8 nm (Fig. 1), and was synthesized by wet precipitation method (Ref 34). HA powders were first dispersed in acetone through probe sonicator

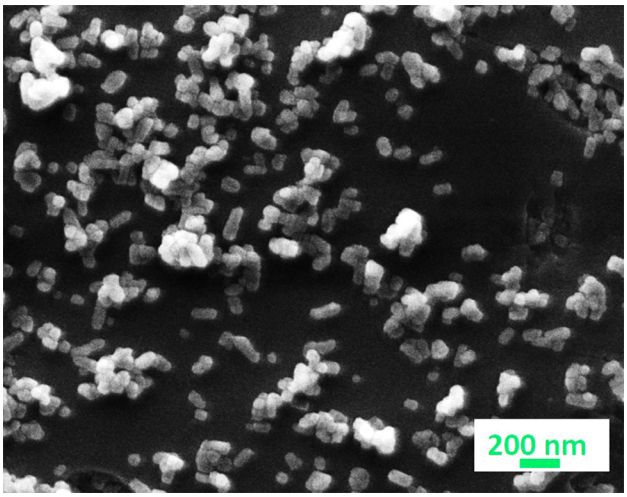

Fig. 1 FE-SEM micrograph of hydroxyapatite powder (cylindrical shape length of 180 ± 20 nm and diameter of 83 ± 8 nm)

(PKS-750FM, PCi Analytics, Mumbai) with the frequency of 20 kHz for 20 min followed by the addition of 3 wt.% zinc and balanced magnesium and then further sonicated for 40 min for better dispersion (Ref 30). The powders were compacted and sintered using spark plasma sintering (DR SINTER625, Japan). The powder was placed in a die made of grade 2333 graphite (MERSEN d. Carbone Lorraine). Due to the low sintering temperature, instead of a graphite foil, boron nitride was applied on the punches, using boron nitride spray (Kontakt Chemie). Two-stage sintering was carried out in vacuum (6 Pa) at two different temperatures of 450 °C and 500 °C with holding time at each stage of 5 min, for better densification. The heating rate and compaction pressure were 50 °C/min and 80 MPa, respectively. The samples are named as MZ, MZ5H, MZ10H, MZ15H and MZ20H based on the content of HA reinforcement in wt.%.

2.2 Physical Characterization of Powders and Composite

Optical microscope (Leica, DMI 5000 M light optical microscope) was used to observe the microstructure of sintered samples. The grain boundaries were observed in the samples after etching with 2 g of picric acid and 50 ml of ethanol (Fig. 4a). Helium pycnometry (Smart Instrument Co. Pvt. Ltd. Maharashtra) was used to determine the density of sintered samples. Phase structure of the powders and sintered composites were analyzed by x-ray diffractometer (XRD; smart lab, Rigaku, Japan). The x-ray diffractometer analysis was done at 2θ range of 20° to 80° with 1 °/min scan rate by using Cu Kα (λ = 1.5418 Å) radiation. The surface micrographs of degraded composites, after exposure, and composition of corroded products were examined by field emission scanning electron microscopy (FESEM; Carl Zeiss ultra plus, Germany) and energy-dispersive spectroscopy (EDS) (FESEM; Carl Zeiss ultra plus, Germany), respectively.

2.3 Characterization of Degradation Behavior

2.3.1 Electrochemical Test. Accelerated corrosion tests were performed at 37 ± 1 °C temperature using an electrochemical workstation (Interface1000, Gamry Instruments, USA) with 0.5 mV/s^1 scan rate. The range of potential was swept from 250 mV above and 250 mV below the open circuit potential (OCP). The three-electrode cell was used, in which standard calomel electrode SCE (+ 0.242 V vs. standard hydrogen electrode) was used as the reference electrode with platinum as counter electrode and Mg-3Zn/HA specimen as the working electrode. The cell had 0.785 cm^2 window for exposing the specimen surface to the corrosion medium, which is simulated body fluid (SBF) in this case. Kokubo's recipe was used to prepare SBF (Ref 35). Before the experiment, all the specimens were metallographically polished up to 2000 grit size using SiC emery paper. The sample was given 1800 s to stabilize the OCP. The experiments were repeated at least three times, and then average values were reported. The electrochemical parameters (E_{corr} and I_{corr}) were obtained from the Tafel curve extrapolation.

2.3.2 Immersion Corrosion Test. ASTM-G31-72 standard was followed to evaluate in vitro degradation rate and bioactivity. Disk shape samples were cut into two halves and were metallographically polished till 2000 grit size, followed by polishing with 0.2 and 1-µm diamond paste. Further, the samples were dipped into SBF, in sterilized glass vials at 37 ± 1 °C. The temperature was maintained through incubator. The samples were retrieved after different immersion duration of 3, 7, 14, 28 and 56 days. Retrieved samples were washed gently with distilled water and dried in desiccators for 48 h. FESEM was used to observe the surface morphology of the retrieved samples. To evaluate the apatite precipitation kinetics, the weight of the specimens was recorded prior and subsequent to the exposure in SBF. In order to calculate the degradation rate, the corrosion products, on the surface of the specimens, were cleaned with chromic acid (180 g/L) and weighed again. The Mg^{2+} ion concentration, liberated during exposure, was calculated by inductively coupled plasma mass spectrometry (ICP-MS) (Avanta M, GBC Scientific equipment Pvt. Ltd., Australia) of the immersion fluid. The calibration of the ICP-MS system was done through three solutions of magnesium standard (NIST-certified "CER-TISOL" 1000 mg/L in nitric acid, Mumbai), with concentration of 0.1, 0.2 and 0.4 ppm.

2.4 Mechanical Characterization

The hardness test was performed using Vickers's hardness tester (FEI-VM 50PC, Tal. Shirol, India) using 1 kg load with 15 s of dwell time at peak load. A minimum of 15 indents throughout the composite surface were made on each specimen to get an average hardness value. Compression tests were performed at room temperature on H25 K-S Tinius Oslen compression testing machine (Pennsylvania, USA). ASTM E9-09 standard was followed to perform for compression strength. Cylindrical specimens (8 mm diameter and 12 mm height) were fabricated through SPS to carry out the compression experiments. Cross-head speed during compressive tests was 10^{-4} mm/s, and strain rate was 0.08 s^{-1}. Three specimens were tested for every composition.

2.5 Contact Angle Measurement

The sessile drop method technique was used to measure the contact angle (θ) for all the specimens at environment temperature (25 °C) with contact angle goniometer (KRUSS, DSA25 Germany). Simulated body fluid was chosen to make sessile drop. The sessile drop was formed by using automatic microsyringe by placing 2 µl constant drops of the SBF.

2.6 Biocompatibility and Cell Culture Test

2.6.1 Human Osteoblast Cell Culture. Human fetal osteoblast progenitor cell (hFOB) was obtained from Central Drug Research Institute (CDRI), Lucknow, India. The cells were cultured in Dulbecco's modified Eagle's medium (DMEM)/F-12, GlutaMAX™ (Gibco, Life Technologies, USA) with 10% fetal bovine serum (FBS) (heat-inactivated) (Invitrogen, Carlsbad, CA, USA), 1% antibiotic (100 U/ml of penicillin and 100 µg/ml streptomycin) (Hi-Media, India) and 0.3 mg/ml Geneticin (Gibco, Life Technologies USA). The cultured cells were maintained at 33.5 °C in a humidified incubator under a 5% CO_2 atmosphere. After every 48 h, the cells were subcultured. For sub culturing, the cells were harvested from subconfluent cultures (60-70%) using 0.25% trypsin–EDTA (Gibco, Life Technologies, USA).

2.6.2 DAPI Staining. To check the effect of growing cells on implants on their proliferation, the cells grown on implants were fixed with 3.7% formaldehyde after 3 and 5 days of culture and stained with 4′,6-diamidino-2-phenylindole (DAPI, Sigma, USA). The images were captured using a fluorescence microscope (Carl Zeiss Axiovert 25, Germany).

2.6.3 Cell Viability Assay (MTT assay). 3-(4, 5-Dimethylthiazol-2-yl)-2,5-diphenyltetrazolium bromide (MTT) reagent was procured from Himedia, India. The MTT assay was used to estimate the cell viability, based on NAD(P)H-dependent cellular oxidoreductase mitochondrial enzyme. The cells, which are viable, have the potential to transmute tetrazolium salt into purple formazan crystals. The seeding of hFOB cells was done on to the implant(s) in 24 well plate (Corning, Costar, NY) at a density of 20,000 cells per well and incubated for 1, 3 or 5 days. On completion of the respective incubation periods, fresh 400 µL DMEM medium, along with the MTT dye (0.5 mg/mL^1), was added into each well and incubated for another 4 h. Finally, 400 µL of DMSO solution was added to dissolve the formazan crystals formed, after the medium was aspirated. The optical density (OD) of the resulting purple solution was measured at 570 nm in a plate reader (Fluostar Optima, BMG Labtech, Germany) and used to calculate the percentage of cell survivability as:

$$\%\text{Cell Survival} = \frac{\text{OD from cells grown on implant}}{\text{OD from cells growm on regular tissue culture well}} \times 100$$

Before performing MTT and DAPI staining, the implants were preconditioned by incubating. The composite specimen was kept in SBF for 2 days, followed by immersing them in DMEM-F12 cell culture media for 1 day.

2.6.4 Statistical Analysis. Statistical analysis was performed using Graphpad Prism 5.04 (GraphPad Software, San Diego, CA, USA). Data were represented as mean ± standard error. For statistical analysis, one-way ANOVA was used. The level of statistical significance was set at $p < 0.05$.

3. Results and Discussion

3.1 Characterization of the Sintered Compacts

Figure 2 shows schematic representation of sintering schedule followed in synthesizing Mg-3Zn/HA composite samples using SPS technique. The SPS sintering was selected as it offers innumerable benefits, e.g., better densification and mechanical properties. Apart from these, SPS also helps in homogeneous and uniform microstructure development, which ultimately helps in corrosion resistance. Two-stage sintering profile was followed to compact the samples. First-stage sintering at 450 °C enables electric discharge induced surface activation, while second-stage sintering at 500 °C promotes grain boundary diffusion-induced neck growth formation. This leads to complete densification of metal and ceramic, by plastic deformation of softened Mg, which has melting point of 650 °C (Ref 36).

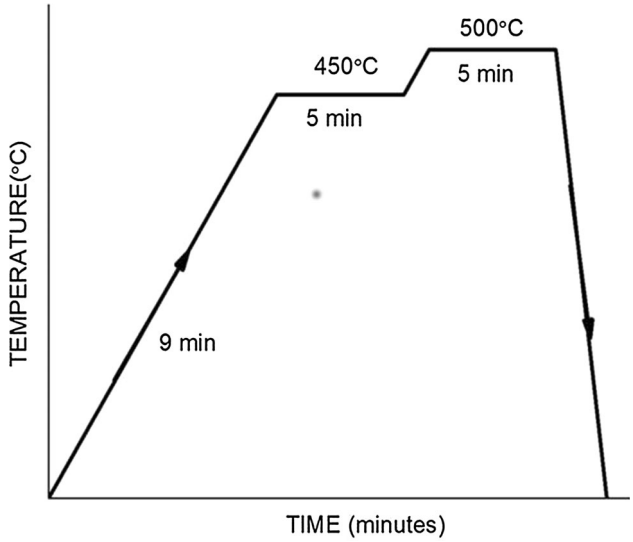

Fig. 2 Schematic representation of sintering schedule followed in synthesizing Mg-3Zn/HA composite samples using MS-SPS technique

Table 1 Theoretical and experimental density values for composites

Composites	Theoretical density, g/cm^3	Experimental density, g/cm^3	Relative density, %
MZ	1.89	1.81	96
MZ5H	1.96	1.86	95
MZ10H	2.03	1.96	97
MZ15H	2.11	2.06	98
MZ20H	2.17	1.97	91

Table 1 presents density values for the composites. The density of Mg, Zn and HA as 1.71 g/cm^3, 6.61 g/cm^3 and 3.11 g/cm^3, respectively, is considered while calculating % theoretical density (TD). It was noted that the relative density was low for MZ20H composites, as compared to other composites. High melting HA (1100 °C) (Ref 37) does not interact intensively with Mg particle at lower sintering temperature (450 and 500 °C). Figure 3 shows the XRD pattern of the sintered Mg-3Zn/HA composite and the Mg, Zn and HA powders. The XRD pattern depicts that all the consolidated specimens follow similar pattern with the changes in relative intensities as HA content increases. Quantity of non-diffused HA particles increases with its content in the composite structure. Hence, densification is poor and thus leads to porosity

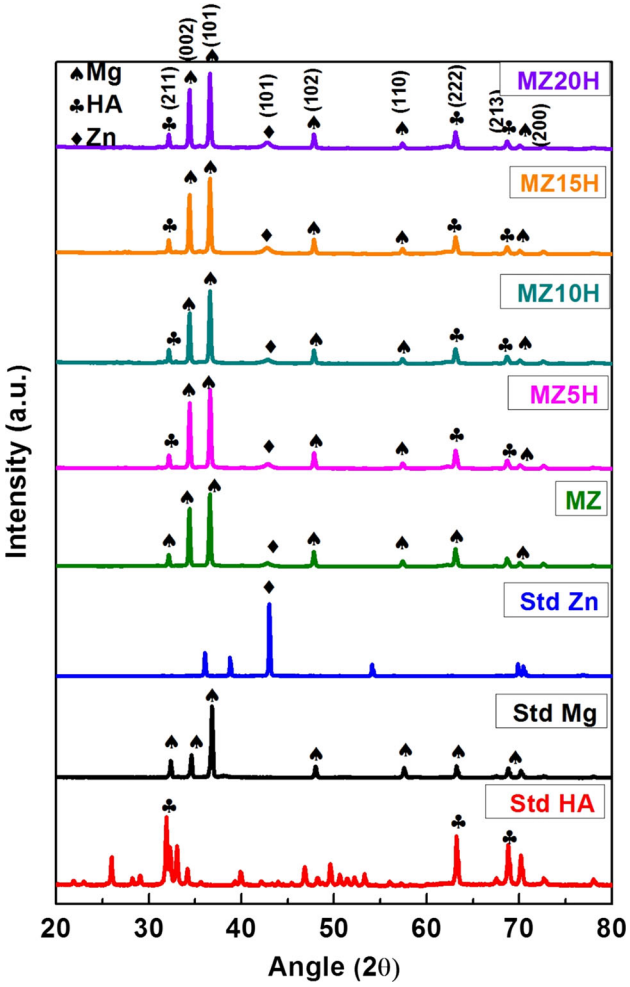

Fig. 3 XRD patterns of the sintered composites

in the composites, which can be clearly confirmed through dark patches present in the optical microscopic images shown in Fig. 4.

Peaks of all the elements were found in the XRD pattern (Fig. 3) and have been shown with different symbols. The peak of Mg, in MZ15H composite, corresponding to angle 34.40° shows higher intensities. This increment in intensities can be attributed to the expansion of the fraction of the grains oriented with the basal planes in compaction direction (Ref 36).

3.2 Morphology of Sintered Composites

Figure 4 shows optical micrographs of MZ, MZ5H, MZ10H, MZ15H and MZ20H composites, fabricated by SPS. Mg grains are being represented by gray color, while the black color represents HA. However, pores might also be represented by black color in bright-field images. Thus, the dark-field image of MZ15H is presented in Fig. 4(e), which shows HA as white spots. This image confirms majority of dark spots in bright-field optical images are from HA and not from pores. MZ shows almost no pores along the grain boundary. Zn particles are not visible from all the optical images, due to small percentage of zinc (3 wt.%) being added to the composites. HA (black color) can be observed near the grain boundaries of Mg matrix. Figure 4(d) shows the microstructure of MZ15H with minor agglomeration or clustering of the HA particulates, as compared to MZ20H. The clustering of HA is indicated by red circle in respective micrographs. A severe agglomeration can be seen in MZ20H, owing to higher weight percentage of HA. Deterioration of mechanical properties of MZ20H can be attributed to these severe agglomerations as shown in Figs. 5 and 6. The clustering of HA leads to formation of larger pores at the interface of HA/HA and magnesium/HA. However, confirms overall better diffusion, as well as densification of the composites during sintering process (Fig. 8).

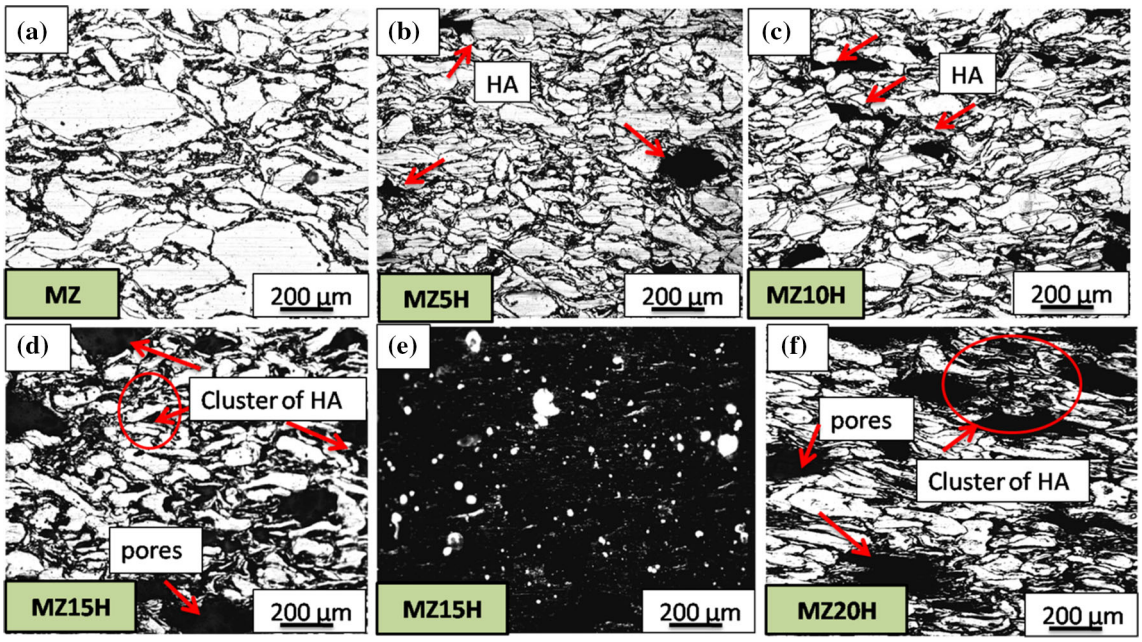

Fig. 4 Optical micrographs of the composites (a) MZ, (b) MZ5H, (c) MZ10H, (d) MZ15H, (e) dark-field MZ15H and (f) MZ20H (Red circle denotes the agglomeration of HA)

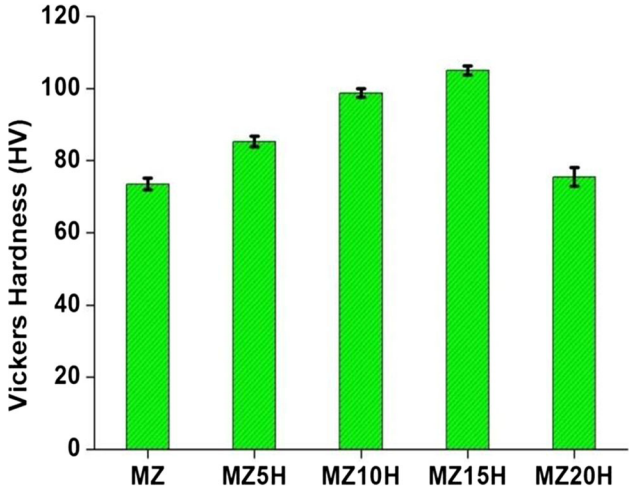

Fig. 5 Vicker's hardness values of composites having different HA compositions

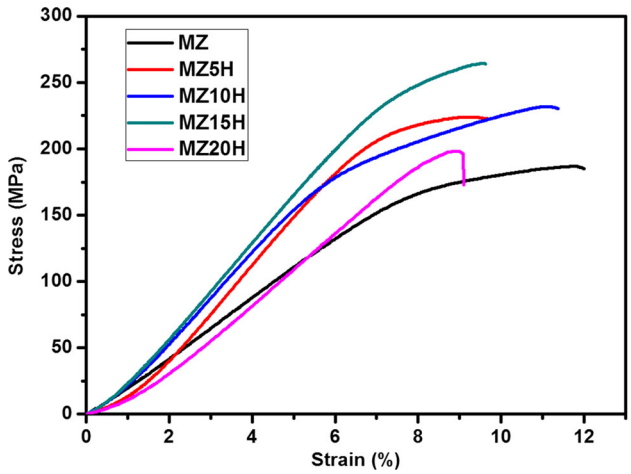

Fig. 6 Representative plots from compressive stress–strain studies for all compositions

3.3 Mechanical Behavior of the Composite

Hardness, as a function of HA content, is shown in Fig. 5. Hardness gradually increases with HA content. MZ15H has shown a maximum of ~ 42.8% increment in hardness as compared to MZ. This tendency was also observed by others on reinforcing Mg with HA (Ref 30, 31). The error bars in Fig. 5 indicate standard deviation in measured hardness values. Very small error bars denote uniform mechanical behavior of the composites at micrometer level. The improvement in hardness is attributed to the reinforcement effect from harder HA phase (hardness 5.272 GPa) in softer Mg matrix (hardness 0.44 GPa) (Ref 30). But there was a significant drop in hardness in composites beyond 15 wt.% HA content. The MZ20H composite has shown comparatively less hardness. As it was previously demonstrated, the incorporation of higher content of reinforcement provokes non-uniform dispersion throughout the composite, which might cause the anomalous performance of composites (Ref 22, 30). The improvement in composite's surface resistance property can also be attributed to the progressive consequence of work hardening evolved because of the various particles size and dissimilar phases like Mg, Zn and HA inside the hybrid composite. Uniformly distributed HA reinforcement shares the load transferred from the Mg matrix and resists deformation. Agglomeration of HA generates irregularity and porosity inside the composites, which may be the reason for 22% decrement in hardness value of MZ20H, as compared to MZ15H.

The representative stress–strain plots from compression tests for all the spark plasma sintered compacts are presented in Fig. 6. The compressive yield strength calculated at 0.2% of the plastic deformation is shown in Table 2. The compressive yield strength of MZ is ~ 27% lower than the that of composites containing 15 wt.% of hydroxyapatite (HA), while MZ15H showed highest ultimate compressive strength (257.03 ± 5.4 MPa) as compared to other composites (~ 18% greater than MZ). This can be attributed to uniform and better distribution of HA as reinforcement in Mg matrix. Higher compressive strength of HA (~ 700 MPa (Ref 4)) can positively influence the mechanical property of composites. SPS enables faster densification and higher level establishment of inter-particle atomic bonding, at comparatively lower temperatures, by faster heating the powder particles surfaces at the inter-particle grain boundaries and efficiently removing oxide layer from metallic surface and ceramic particles, through electrical sparking. This entire phenomenon, cumulatively, could improve the interfacial bonding between the MZ matrixes and HA reinforcement. This better interfacial bonding and uniform dispersion of HA might be the reason of significant improvement in the ultimate compressive strength of the entire composite with up to 15 wt.% of HA addition. On the contrary, in case of conventional sintering, HA reinforcement was limited to 5 wt.% in Mg-3Zn matrix and beyond that mechanical and corrosion properties started deteriorating (Ref 31). Similar trends were observed in hardness and compression strengths. In addition to that, the average grain size refinement of magnesium can also improve the yield strength, which can be accomplished through minimizing the activity of twinning. In the present research, the addition of 15 wt.% HA reinforcement contributed to the higher average strain endured in the grains of the Mg matrix. This may be the reason for impeding the crack propagation and the increase in the fracture energy of

Table 2 Mechanical properties of composites obtained from uniaxial compression tests

Composites	0.2%YS, MPa	Ultimate compressive strength, MPa	Failure strain, %	Toughness, J/m^3
MZ	103.8 ± 1.3	217.2 ± 4.4	13.1	140.9
MZ5H	111.8 ± 3.2	230.1 ± 5.9	14.6	126.8
MZ10H	120.1 ± 3.9	242 ± 2.7	16.1	165.8
MZ15H	131.7 ± 2.6	257.3 ± 5.4	17.5	143.7
MZ20H	97.5 ± 1.8	207.2 ± 4.3	13.2	89.2

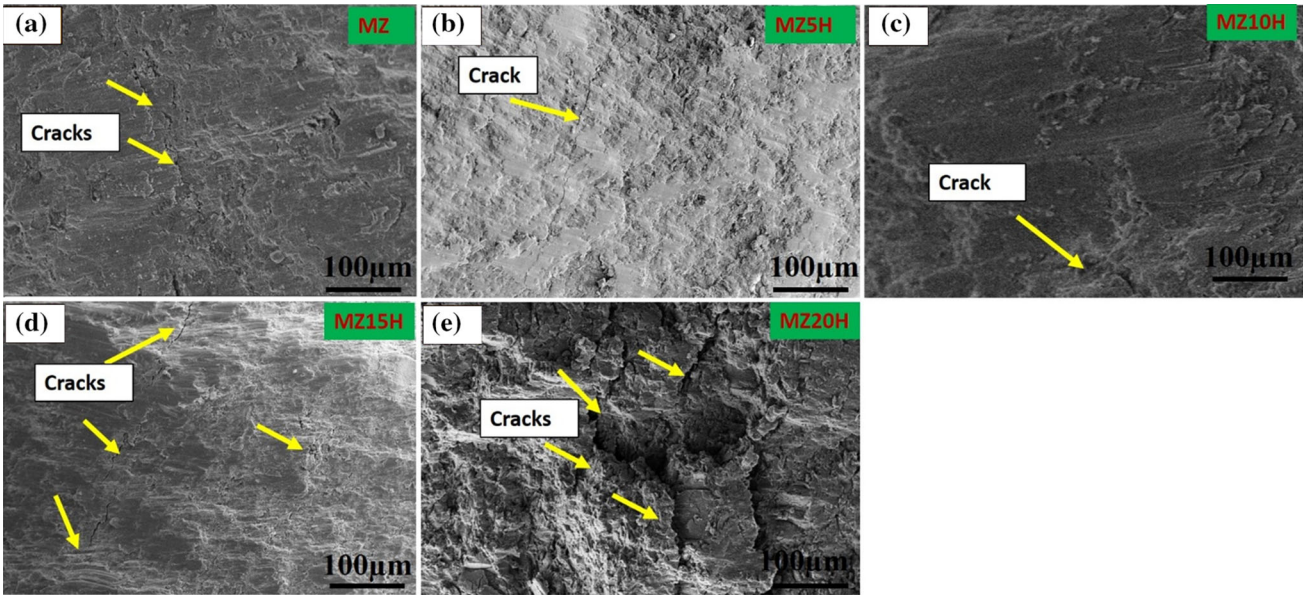

Fig. 7 FESEM images of the compressive fractured surfaces of the composites (a) MZ, (b) MZ5H, (c) MZ10H, (d) MZ15H and (d) MZ20H (the arrows denote cracks)

Mg-3Zn/HA composite. However, incorporation of 20 wt.% HA in composite unveils a remarkable drop of ~ 14% in ultimate compressive strength. The higher addition of HA contents leads to agglomeration of particles. Agglomeration of particles contributes in increasing the porosity of composites, which ultimately deteriorates the mechanical and corrosion behavior of composites. In addition to this, at higher content of HA (> 20 wt.%), the population of agglomerated HA particles increases, which does not make good inter-atomic bonding with matrix. This might be the reason for deteriorating the property of 20 wt.% HA. Further, HA, being brittle in nature, leads to fragility of composite with agglomeration. This leads to the early failure of 20 wt.% HA-containing composite. Failure strain is reduced by ~ 27% with 20 wt.% HA reinforcement, as compared to the MZ composite. On the other hand, failure strain with 15 wt.% HA composition was ~ 25% higher as compared to 20 wt.%. It recommends that the addition of HA reduces the compressive failure strain of the magnesium materials.

Figure 7 shows the FESEM micrographs of the compressive fractured surface of the composites. Fractured surfaces clearly show good sintering and bonding of the particles. No single particle is observed to be coming out from the fractured surface, which confirms better diffusion and densification of the composites, during sintering process. The fractured surfaces of the composites do not reveal ductile dimples. Mostly, all the composites show similar compressive fractured surfaces. Fine cracks are visible on the composite surfaces and morphology appears to be smooth, which indicate quasi-cleavage fracture mode. However, at higher concentration of HA (20 wt.%), larger cracks and very rough fracture surface are observed. This is probably due to the agglomeration of HA particles at high content. Upon application of compressive load, the stress concentration due to agglomerated HA particles leads to crack propagation and brittle fracture. Figure 8(b-f) depicts the elemental mapping of the fractured surface of 15 wt.% HA composite. Cumulative and discrete dispersion of elements has been shown with different colors. Elements are found homogeneously dispersed in appropriate compositions. This is reason for having smoother fracture surface and finer cracks in Mg/3Zn matrix, up to 15 wt.% HA content.

3.4 Corrosion Analysis

3.4.1 Potentiodynamic Polarization Test. Biodegradable Mg-based composite materials, implanted in the body, will react with the surrounding medium. In this process, implant gradually degrades over time and gets absorbed into the body. However, a very fast degradation deteriorates the structural integrity of the implant, thus making it unsuitable for load-bearing application, even during its active requirement period. Thus, it is important to understand the corrosion behavior of the composites in simulated in vivo environment. Figure 9 shows the representative Tafel curves for potentiodynamic polarization test of all the composites in simulated body fluids. In general, the oxidation reaction of Mg^{2+} ions correlates the anodic current density. On the other hand, the reduction reaction of water in hydrogen gas evolution reaction correlates with the cathodic current density (Ref 38).

$$\text{Anodic reaction: } Mg \rightarrow Mg^{2+} + 2e^{-}$$
$$\text{Cathodic reaction: } 2H_2O + 2e^{-} \rightarrow H_2 + 2OH^{-}$$

In the present study, corrosion current density (I_{corr}) was calculated by Tafel extrapolation technique through a linear region of cathodic polarization curves. The potential of corrosion (E_{corr}) and current density of corrosion (I_{corr}) of the all specimens are enclosed in Table 3. A decrement in (I_{corr}) and shifting in (E_{corr}) toward positive side were observed with the addition of HA in matrix. An improvement in corrosion resistance by ~ 60% is noticed with addition of 15 wt.% HA. However, MZ20H shows the poor corrosion rate in comparison to other composites. Incorporation of higher content of HA leads to the clustering tendency of nano-size particulate, which resulted in clustering-related porosity. These pores and clusters are secondary phase particles and corrosive sites for Mg. There are some studies available corroborating this observation that

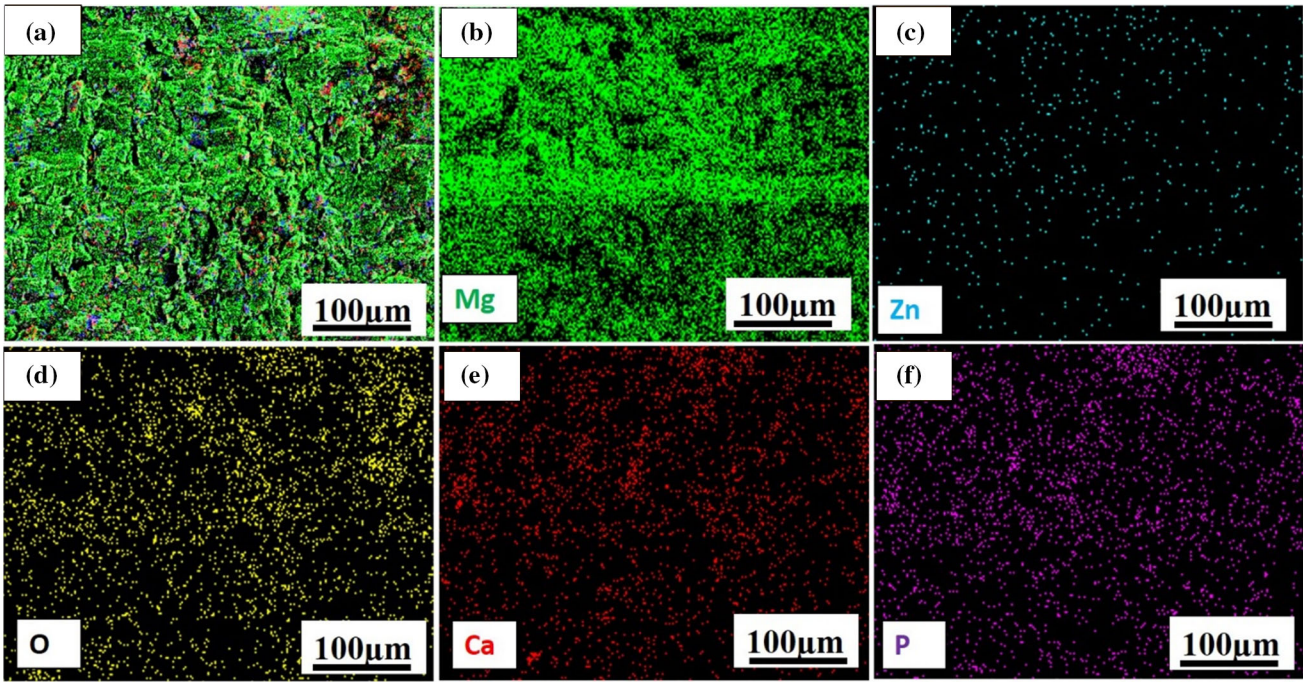

Fig. 8 EDS analysis of fractured surfaces, (a) cross section image of 15 wt.% HA, (b-f) elemental mapping of MZ15H composite's fractured surface

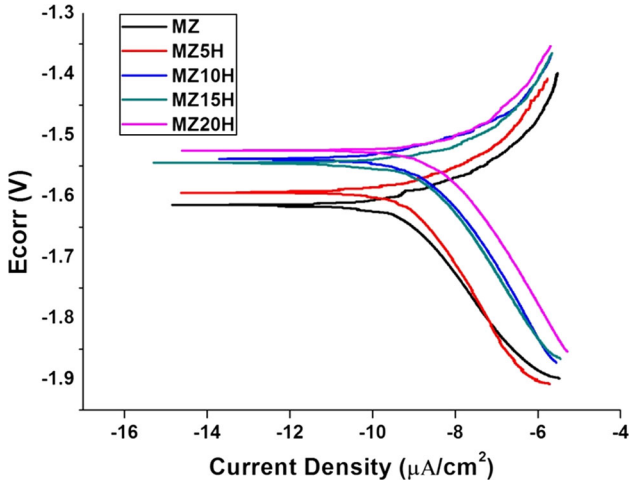

Fig. 9 Representative potentiodynamic polarization curve of the composites

higher content of HA is more prone to localized pitting corrosion of magnesium (Ref 39). In some studies, addition of HA > 10 wt.% caused higher corrosion rate (Ref 15, 24, 30, 33). The corrosion rate of Mg-based composite can be decreased with optimized quantity and uniform distribution of HA. The ceramic nature and higher melting temperature of HA do not offer much interaction with Mg at low sintering temperature. The problem becomes severe at high HA content. If HA does not diffuse with Mg matrix and forms agglomerates, there will be an increase in galvanic couple throughout the exposed surface, leading to higher corrosion sites. In connection to this, the shape and distribution of HA particles determine the corrosion resistance. The same trends were found in the present study, as addition of 20 wt.% HA causes

Table 3 I_{corr} and E_{corr} values of all the composites

Samples	E_{corr}, V	I_{corr}, µA/cm^2	Corrosion rate, mpy
MZ	− 1.61 ± 0.05	229.2 ± 8.7	183.4
MZ5H	− 1.59 ± 0.06	215.2 ± 7.5	165.3
MZ10H	− 1.55 ± 0.04	193.6 ± 6.7	140.6
MZ15H	− 1.51 ± 0.04	164.3 ± 4.9	73.51
MZ20H	− 1.52 ± 0.06	363.5 ± 16.3	299.8

an increase in intensity of the galvanic couple as HA is agglomerated and unevenly distributed in that composition. The agglomeration further leaves the Mg matrix devoid of HA also. Reinforcement of 15 wt.% HA in Mg-3Zn contributed in increasing the corrosion resistance of Mg-3Zn by ~ 60%. The corrosion resistance is optimized with the proper amount and uniform diffusion of Zn and HA. The noble behavior, shown by MZ15H, could be attributed to better distribution and also optimized content of HA in Mg matrix.

3.4.2 Immersion Testing. Generally, the conventional corrosion experiments, such as potentiodynamic polarization testing, are of great value for the evaluation of the potential of a composite to corrode. However, they need to be complemented by long-term immersion tests to have an in-depth analysis of in service corrosion behavior of degradable temporary implants. Immersion test offers an insight into the degradation rate and bioactivity of any materials in vitro. Considering this fact, long-term static immersion tests of the composites are performed in simulated body fluid (SBF) over a period of 8 weeks.

After retrieving the composite from SBF, they are cleaned with distilled water and kept for drying for 2 days in desiccators. The composites were weighed again with the layers on them to measure the mass gain. Figure 10 shows the relationship between the weight gain of the composites after

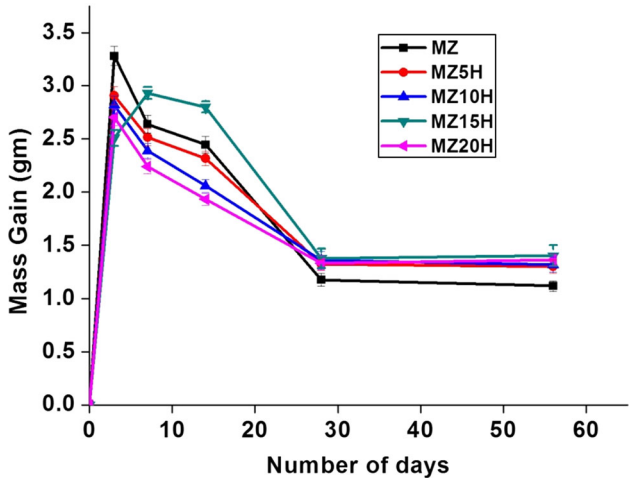

Fig. 10 Mass gains of different compositions as a function of SBF immersion time

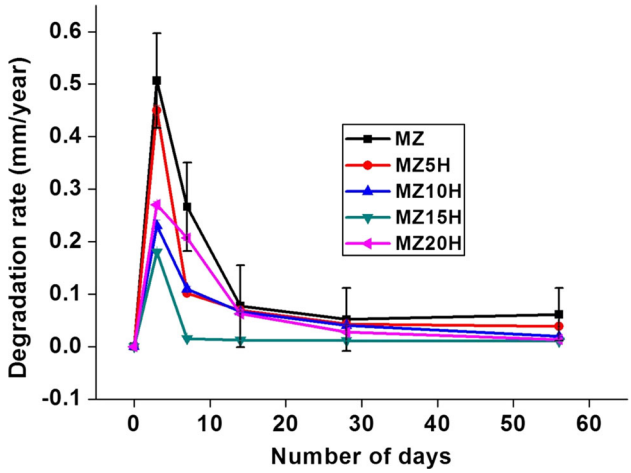

Fig. 11 Degradation rate of composites as a function of SBF immersion time

immersion into SBF as a function of immersion period (3, 7, 14, 28 and 56 days).

After weighing, the samples were dipped into CrO_3 solution to remove corrosion precipitates on the surface of the composites and then weighed again to assess the degradation of Mg matrix. Figure 11 shows the degradation rate for all the composites after exposure into the simulated body fluid for different periods of time (3, 7, 14, 28 and 56 days).

Figure 12 presents the Mg^{2+} ion concentration in SBF, collected after the immersion studies for different time duration. The concentrations of Mg^{2+} ion were evaluated through inductively coupled plasma mass spectrometry (ICP-MS). The Mg^{2+} ion concentration was higher for MZ composites, without any HA reinforcement.

Gain in the mass of composites was observed in physiological environment due to the apatite layer growth on the specimen's surfaces. It was found that apatite layer growth rate increases with HA content up to 15 wt.%, after which a decrement in the apatite layer formation was observed. In addition to that, during initial 3 days of exposure, the rate of apatite formation was significantly higher as compared to

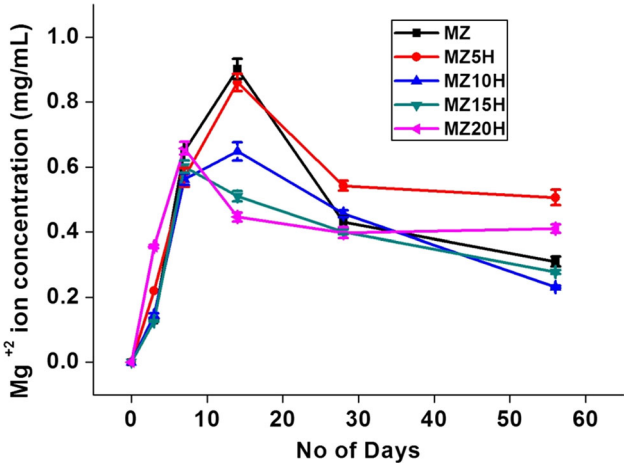

Fig. 12 Concentration of Mg^{2+} in retrieved SBF from the immersion testing

further immersion periods. Finally, the rate became almost constant after 28 days of exposure (Fig. 11). Formation of more apatite layer with respect to days of immersion might be the reason for decrease in degradation rate of MZ15H composites.

Initially, the degradation rate was highest for MZ. But after 28 days of exposure, it became almost consistent up to 56 days. The extended soaking time in simulated body fluid leads to the reduction in degradation rate but causes increment in pH level of the solution. In addition to that, apatite layer growths on the surface help to lessen the degradation rate. In the present context, MZ15H is showing the lowest corrosion rate and also highest amount of apatite layer formation. The composition of reinforcement, exposed area, density and morphology of the immersed samples cumulatively affects the apatite layer formation on the composite. The bioactive nature and homoepitaxy with HA support apatite layer precipitation. But, after a certain composition of reinforcement in composites, HA starts forming clusters, leaving HA-depleted region in the matrix. This results in less apatite coverage on those areas, ultimately deteriorating the degradation resistance of the composite. This may be the reason for deteriorating property of the 20 wt.% HA samples.

The oxidation of Mg was greatly affected by high concentration of buffering agents present in body plasma. The following reaction takes place when Mg is exposed to an aqueous solution,

$$Mg + 2H_2O \rightarrow Mg^{2+} + 2OH^- + H_2$$

The buffering agents consume the generated OH^- quickly in turn, expediting the conversion from Mg to Mg^{2+}. As recorded in Fig. 11, oxidation rate of Mg^{2+} ions in simulated body fluid was high for initial days of exposure due to apatite growth on the substrate. The oxidation rate started decreasing after 7 days of exposure. Growth of apatite layer on the surface of composites helps in decreasing the degradation rate, by creating an inert shielding.

Figure 13 is depicting the FESEM images of composites for different days of immersion. It can be observed from micrographs that HA content helps in growth of apatite layer. It also depends on the number of days of exposure, as more apatite layer growth was observed on 28 days of immersion for

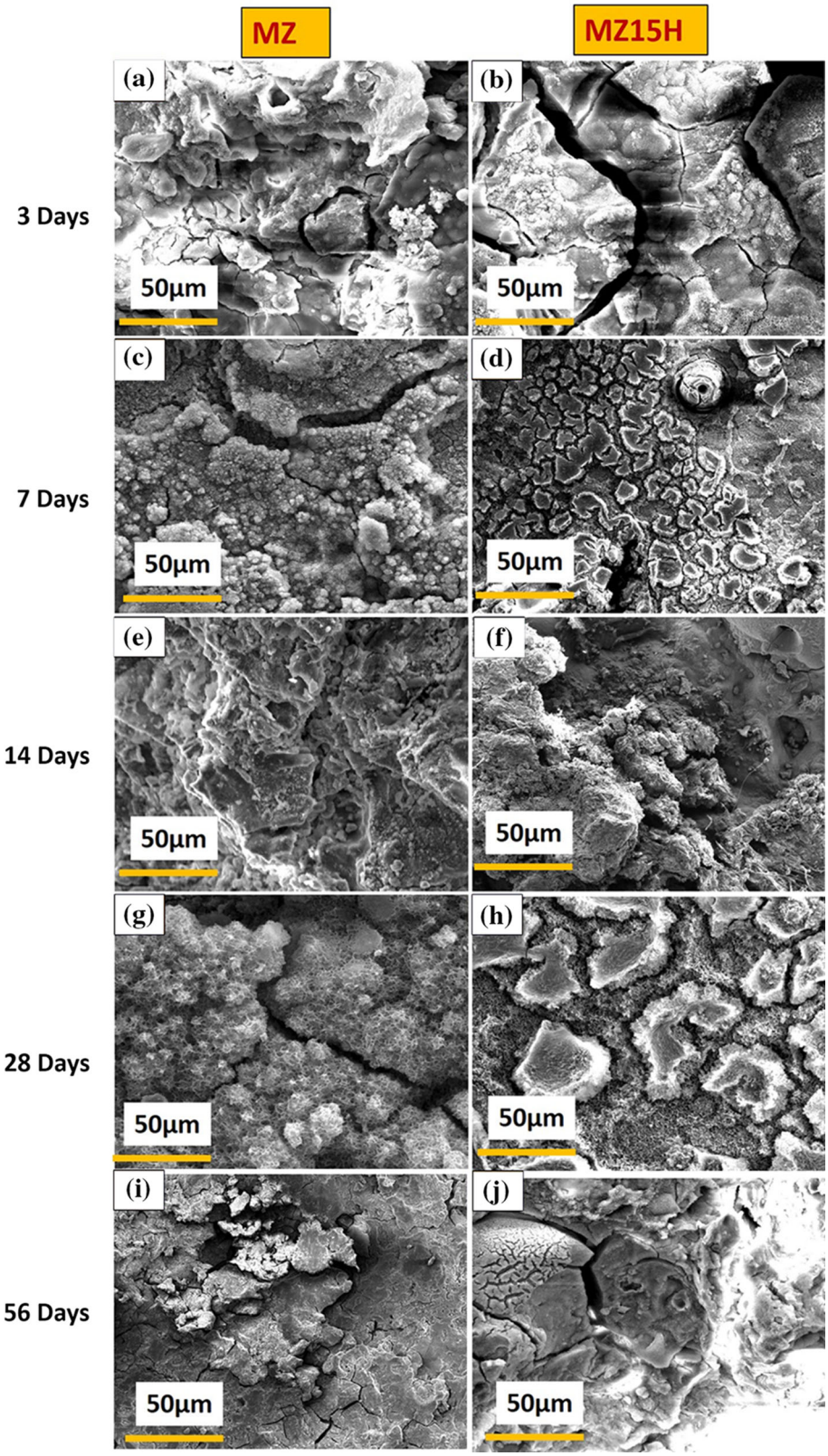

Fig. 13 SEM micrograph of composite structures immersed for (a, b) 3 days, (c, d) 7 days, (e, f) 14 days, (g, h) 28 days and (i, j) 56 day

MZ15H composite (Fig. 13h) than on MZ (Fig. 13c). The optical microstructure of MZ15H in Fig. 4(d) and (e) has shown high degree of HA dispersion throughout the composite, which helps in more nucleation of apatite. The overall apatite layer growth was more on MZ15H composite and can be clearly seen from the microstructure (Fig. 13b, d, f, h, j), as compared to MZ, which tailored the degradation behavior of composite.

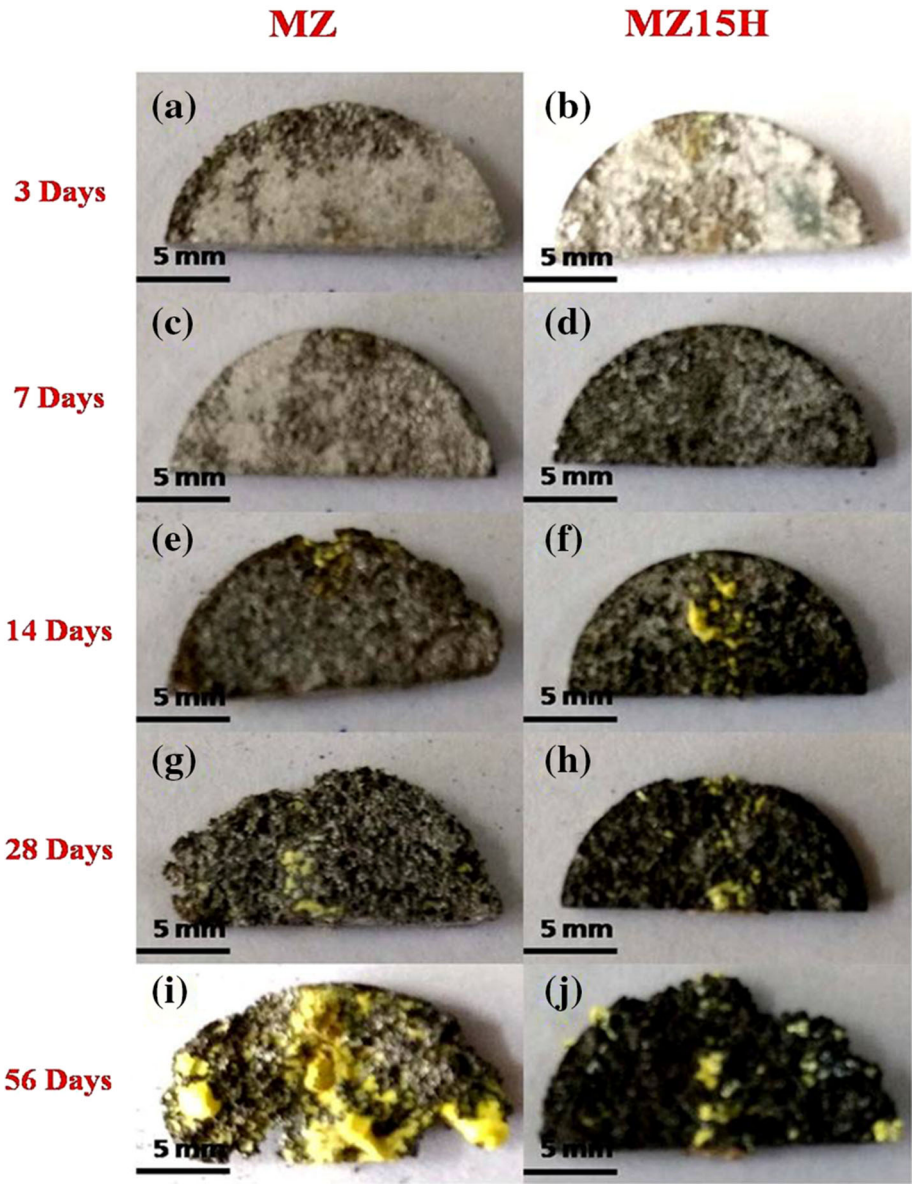

Fig. 14 Digital images of composite structures immersed for (a, b) 3 days, (c, d) 7 days, (e, f) 14 days, (g, h) 28 days and (i, j) 56 days, respectively, after removal of apatite layers from chromic acid

Figure 14 presents the digital images of the composites with various periods of exposure and after removal of apatite layer. It can be clearly seen that MZ reveals small shallow pits after 28 and 56 days of immersion, which are the result of highly localized corrosion (Fig. 14g, i). Their depth increases with the passage of time. MZ composite was more prone to degradation with the increase in the time of exposure. But, the MZ15H composite has shown comparatively better physical integrity and it has survived with less degradation.

3.5 Evaluation of Biocompatibility

Cytocompatibility of the implants was checked on human fetal osteoblast cells (hFOB), using respective viability (MTT) and proliferation (DAPI staining) assays. The MZ15H surfaces have shown improvement in hFOB cell viability over MZ specimen. Previous studies from our group have reported cell viability and growth for human osteosarcoma cells (MG-63) on solgel (Ref 34) as well as electrophoretic (Ref 39-41) coating of HA on Mg-3Zn alloys. The coating of HA on Mg-3Zn alloy substrate improved the cell adhesion property. The presence of HA and its solubilization into cellular milieu can positively affect protein adsorption and formation of bioorganic compounds, which are known to stimulate cell proliferation and adhesion (Ref 34). However, no significant change was observed between the cytocompatibilities of MZ, MZ5H, MZ10H, MZ15H and MZ20H implants (Fig. 15). Similar extent of cell adhesion and concomitant proliferation was observed for MZ and MZ15H implants after 3 and 5 days of incubation as evident from DAPI-stained cells. However, cell adhesion and proliferation were improved in case of implants, relative to controls, wherein, cells were grown on tissue culture plates (Fig. 16). The route of synthesis adopted here is SPS, which has improved densification and inter-atomic bonding in the implants. Implants with and without HA had the privilege of experiencing these improvements due to identical processing

route. Inter-atomic interactions are known to facilitate cell adhesion (Ref 42). Plausibly, this evoked similar cytocompatibilities and cell adhesion for all the implants irrespective of presence or absence of HA.

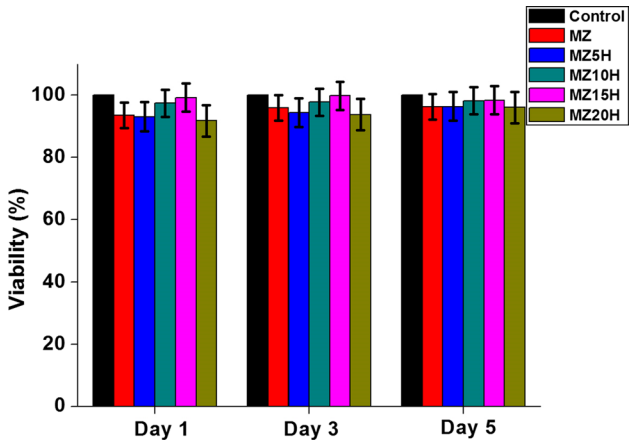

Fig. 15 hFOBcell viability as a function of number of days of incubation, obtained through MTT assay; quantitative representations of MTT assay as % cell survival of hFOB cells grown on different orthopedic implants for 1, 3 and 5 days relative to control cells grown on regular tissue culture petri dish. Data represent mean ± standard error of 3 sets of independent experiments

The contact angle goniometer was used to understand the wettability of surfaces of composites to assess the differential potential of proteins attachment on different compositions, as this is supposedly the reason for difference in cell proliferation and adhesion. Figure 17 presents the measurement of contact angle of MZ and MZ15H composites. The contact angle of water droplet on MZ15H is found to be 55.8° ± 3.3, showing higher hydrophilicity as compared to MZ with contact angle of 83.26° ± 4.1. It is well accepted that better wettability enhances cell proliferation and adhesion. This is due to the presence of fibronectin in cell culture media, which gets adsorbed in higher quantity on hydrophilic surfaces and ultimately enhances the cell adhesion and proliferation in physiological environment (Ref 30).

Thus, MZ15H was found to be suitable candidature for orthopedic applications in terms of improvement in ultimate compressive strength (~ 18%) and degradation resistance (~ 60%), in comparison with other composites. Only one previous report is available on SPS processed Mg/Zn-HA composite. This study (Ref 33) has used 5.5% of Zn in magnesium, which is not suitable quantity according to the literature (Ref 6, 11). The maximum content of HA they could add to magnesium matrix was only 10 wt.%, in comparison with 15 wt.% in the present study, which offered the best properties. The accelerated corrosion data have shown only 49% increase in corrosion resistance (Ref 33). The study has also not carried out evaluation under long-term immersion

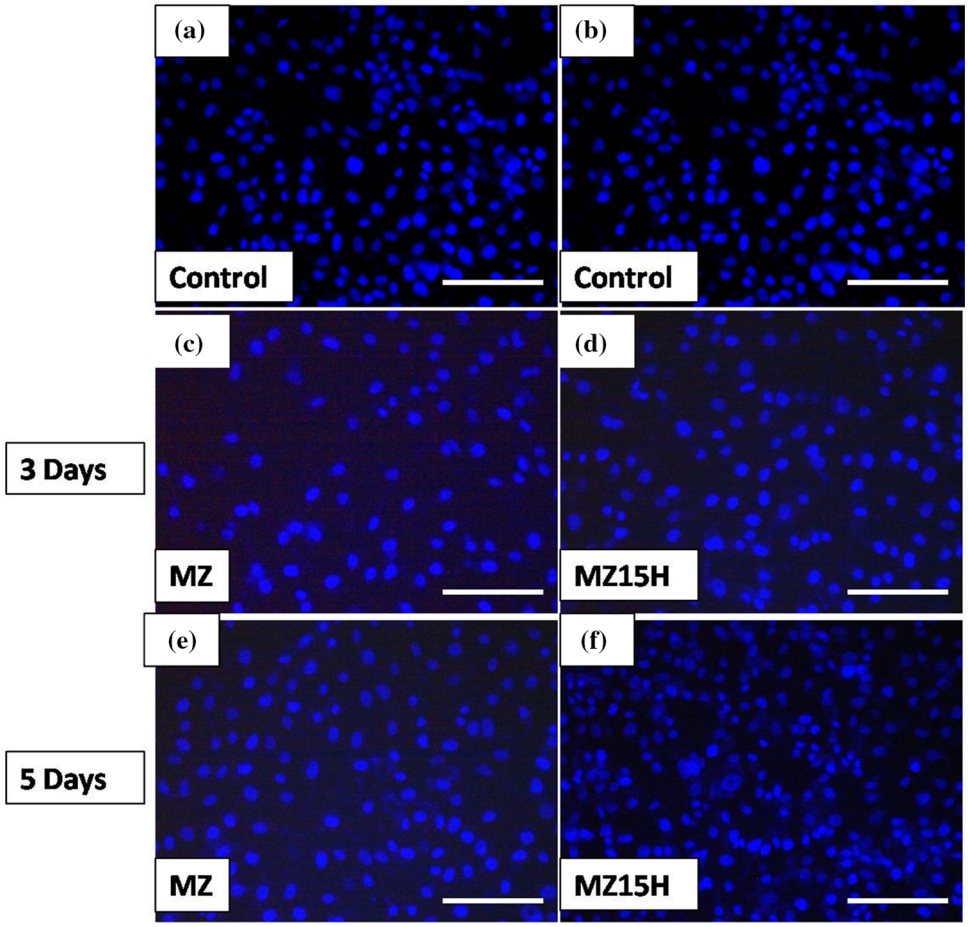

Fig. 16 Fluorescence images of hFOB cells stained with DAPI on third and fifth days after seeding on (a, b) control (tissue culture dish), (c, e) MZ, (d, f) M3Z15H surfaces. Images are representative of three experiments. XXXXX Magnification and scale bar = 100 μm

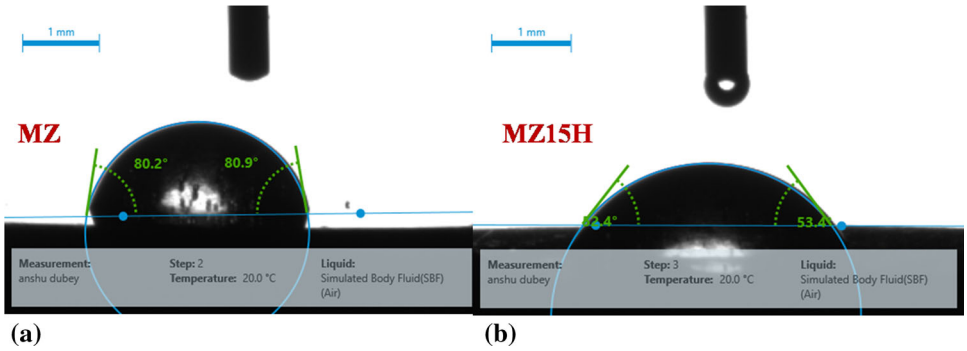

Fig. 17 Contact angles of simulated body fluid drops on M3Z and M3Z15H composite surfaces

condition in physiological environment, which is quite desirable when it comes to magnesium. Long-term exposure to SBF will give an idea whether the implant can be used for in vivo condition. Rather, the same study has reported hydrogen evolution for only 85 h. Further, cell line used for cytocompatibility was mouse fibroblast (L-929), which is not exactly the cell line used for checking osteocompatibility. The present study uses human fetal osteoblast progenitor cell (hFOB) to carry out biocompatibility experiment. hFOB cells offer better understanding of cytotoxicity behavior for Mg implants.

4. Conclusions

In this study, Mg-3Zn/HA composite was successfully fabricated via spark plasma sintering (SPS) route and composites were investigated to for their potential as biodegradable temporary orthopedic implants. The investigations showed that the addition of HA in appropriate amount to Mg matrix could enhance the compressive strength, corrosion resistance and biocompatibility. The composite with the 15 wt.% HA addition offered superior mechanical properties (hardness by $\sim$ 42.8 and compressive strength by 18%), due to the presence of appropriate amount of uniformly distributed HA and better diffusion and compaction of particles obtained by spark plasma sintering. Both electrochemical test and in vitro corrosion evaluation revealed best corrosion resistance for MZ15H composites in SBF. This analysis has revealed that MZ15H wt.% HA offers higher corrosion resistance and their surface stimulates osteoblast cell proliferation and viability. Thus, this study reveals the potential of 15 wt.% HA-reinforced Mg composites as promising material system for temporary orthopedic implants and fracture fixing accessories.

Acknowledgments

DL acknowledges the financial support for funding by DST, India (SB/SO/HS/138/2013). Authors would also like to thank Department of Metallurgical and Materials Engineering, IIT Roorkee for maintaining experimental facilities. The authors would also like to acknowledge Dr. Naibedya Chattopadhyay of Central drug research institute (CDRI), India, for the Human Fetal Osteoblast Progenitor (hFOB) cell line. Thanks are extended to Mr. R Manoj Kumar and Ms. Ankita Bisht, research scholars in the Department of Metallurgical and Materials Engineering, IIT Roorkee, for their technical assistance during experiments. Authors are grateful to the laboratory staff of the Department of Biotechnology, IIT Roorkee, for cell culture facilities.

References

1. M. Saini, Y. Singh, P. Arora, V. Arora, and K. Jain, Implant Biomaterials: A Comprehensive Review 3, *World J. Clin. Cases*, 2015, **3**, p 52-57 (**in Englsih**)
2. N.A. Llah, S. Jamaludin, Z. Daud, M. Zaludin, Mg-Zn Based Composites Reinforced with Bioactive Glass (45S5) Fabricated via Powder Metallurgy, in *AIP Conference Proceedings, The 2nd International Conference on Functional Materials and Metallurgy*, vol. 1756, 2016, p 1-7
3. L. Mao, L. Shen, J. Chen, X. Zhang, M. Kwak, Y. Wu, R. Fan, and W. Ding, A Promising Biodegradable Magnesium Alloy Suitable for Clinical Vascular Stent Application, *Nat. Sci. Rep.*, 2017, **7**, p 46343
4. M. Haghshenas, Mechanical Characteristics of Biodegradable Magnesium Matrix Composites: A Review, *J. Magn. Alloys*, 2017, **5**, p 189-201
5. M.P. Staiger, A.M. Pietak, J. Huadmai, and G. Dias, Magnesium and Its Alloys as Orthopedic Biomaterials: A Review, *Biomaterials*, 2006, **27**, p 1728-1734
6. S. Nayak, B. Bhushan, R. Jayaganthan, P. Gopinath, R.D. Agarwal, and D. Lahiri, Strengthening of Mg Based Alloy Through Grain Refinement for Orthopedic Application, *J. Mech. Behav. Biomed. Mater.*, 2015, **59**, p 57-70
7. G.L. Song and A. Atrens, Understanding Magnesium Corrosion—A Framework for Improved Alloy Performance, *Adv. Eng. Mater.*, 2003, **5**, p 837-858
8. Y.F. Zheng, X.N. Gu, and F. Witte, Biodegradable Metals, *Mater. Sci. Eng. R*, 2014, **77**, p 1-34
9. Z.G. Huan, M.A. Leeflang, J. Zhou, L.E. Fratila-Apachitei, and J. Duszczyk, In vitro Degradation Behavior and Cytocompatibility of Mg-Zn-Zr Alloys, *J. Mater. Sci. Mater. Med.*, 2010, **21**, p 2623-2635
10. D. Liu, M. Chen, and X. Ye, Fabrication and Corrosion Behavior of HA/Mg-Zn Biocomposites, *Front. Mater. Sci. Chin.*, 2010, **4**, p 139-144
11. J. Cheng Gao, S. Wu, L. Ying Qiao, and Y. Wang, Corrosion Behavior of Mg and Mg-Zn Alloys in Simulated Body Fluid, *Trans. Nonferr. Met. Soc. China*, 2008, **18**, p 588-592
12. J. Foltz and C. Blackmon, Metal Matrix Composites, *Adv. Mater. Process.*, 1998, **154**, p 19-23
13. B. Landkof, Development of High Strength Magnesium Based MMC Reinforced with SiC Particles for Satellite Structure Applications, *Material wissenschaft and Werkstofftechnik*, 2003, **34**, p 395-399
14. F. Witte, F. Feyerabend, P. Maier, and J. Fischer, Biodegradable Magnesium-Hydroxyapatite Metal Matrix Composites, *Biomaterials*, 2007, **28**, p 2163-2174
15. A. Han and Y. Feng, The Microstructure, Mechanical and Corrosion Properties of Calcium Polyphosphate Reinforced ZK60A Magnesium Alloy Composites, *J. Alloys Compd.*, 2010, **504**, p 585-593
16. Y. Han and A. Feng, Mechanical and In Vitro Degradation Behavior of Ultrafine Calcium Polyphosphate Reinforced Magnesium-Alloy Composites, *Mater. Des.*, 2011, **32**, p 2813-2820

17. M. Razavi, M.H. Fathi, and M. Meratian, Microstructure, Mechanical Properties and Bio-corrosion Evaluation of Biodegradable AZ91-FA Nanocomposites for Biomedical Applications, *Mater. Sci. Eng. A*, 2010, **527**, p 6938-6944
18. X. Gu, W. Zhou, Y. Feng, Z. Limin, D. Xi, and D. Chai, Microstructure, Mechanical Property, Bio-corrosion and Cytotoxicity Evaluations of Mg/HA Composites, *Mater. Sci. Eng. C*, 2010, **30**, p 827-832
19. Z.G. Huan, M.A. Leeflang, J. Zhou, and J. Duszczyk, ZK30-Bioactive Glass Composites for Orthopedic Applications: A Comparative Study on Fabrication Method and Characteristics, *Mater. Sci. Eng. B*, 2011, **176**, p 1644-1652
20. T. Lei, W. Tang, S. Cai, F. Feng, and N. Liab, On the Corrosion Behaviour of Newly Developed Biodegradable Mg-Based Metal Matrix Composites Produced by In Situ Reaction, *Corros. Sci.*, 2012, **54**, p 270-277
21. Y.F. Zheng, X.N. Gua, Y.L. Xib, and D.L. Chai, In Vitro Degradation and Cytotoxicity of Mg/Ca Composites Produced by Powder Metallurgy, *Acta Biomater.*, 2010, **6**, p 1783-1791
22. A. Khanra, H. Chul, J. Kug, S. Kwang, and S. Shinb, Comparative Property Study on Extruded Mg-HAP and ZM61-HAP Composites, *Mater. Sci. Eng. A*, 2014, **527**, p 6283-6288
23. B. Chen, K. Yin, T. Lu, B. Sun, Q. Dong, J. Zheng, C. Lu, and Z. ChunLi, AZ91 Magnesium Alloy/Porous Hydroxyapatite Composite for Potential Application in Bone Repair, *J. Mater. Sci. Technol.*, 2016, **32**, p 858-864
24. B.R. Sunil, T.S. Kumar, U. Chakkingal, V. Nandakumar, and M. Doble, Friction Stir Processing of Magnesium-Nanohydroxyapatite Composites with Controlled In Vitro Degradation Behavior, *Mater. Sci. Eng. C*, 2014, **39**, p 315-324
25. A. Rahman, Neuropathology of Aluminum Toxicity in Rats (Glutamate and GABA Impairment), *Pharmacol. Res.*, 2003, **47**, p 189-194
26. C. Shuai, Y. Zhou, Y. Yang, P. Feng, L. Liu, C. He, M. Zhao, S. Yang, C. Gao, and P. Wu, Biodegradation Resistance and Bioactivity of Hydroxyapatite Enhanced Mg-Zn Composites via Selective Laser Melting, *Material*, 2017, **10**, p 307-314
27. X. Ye, M. Chen, M. Yang, J. Wei, and D. Liu, In Vitro Corrosion Resistance and Cytocompatibility of Nano-hydroxyapatite Reinforced Mg-Zn-Zr Composites, *J. Mater. Sci. Mater. Med.*, 2010, **21**, p 1321-1328
28. S. Pal, *Design of Artificial Human Joints & Organs*, Springer US, 2014, p 23-40
29. L. Debao, G. Xu, S.S. Jamali, Y. Zhao, M. Chen, and T. Jurak, Fabrication of Biodegradable HA/Mg-Zn-Ca Composites and the Impact of Heterogeneous Microstructure on Mechanical Properties, In Vitro Degradation and Cytocompatibility, *Bioelectrochemistry*, 2019, **129**, p 106-115
30. R.D. Campo, B. Savoini, and G. Garcés, Mechanical Properties and Corrosion Behavior of Mg-HAP Composites, *J. Mech. Behav. Biomed. Mater.*, 2014, **39**, p 238-246
31. S. Jaiswal, M. Kumara, P. Gupta, M. Kumaraswamy, P. Roy, and D. Lahiri, Mechanical, Corrosion and Biocompatibility Behaviour of Mg-3Zn-HA Biodegradable Composites for Orthopaedic Fixture Accessories, *J. Mech. Behav. Biomed. Mater.*, 2018, **78**, p 442-454
32. B. Ratna Sunil, C. Ganapathy, T. Sampath Kumar, and U. Chakkingal, Processing and Mechanical Behavior of Lamellar Structured Degradable Magnesium-Hydroxyapatite Implants, *J. Mech. Behav. Biomed. Mater.*, 2014, **40**, p 178-189
33. C. Zeqin, W. Li, L. Cheng, D. Gong, W. Cheng, and W. Wang, Effect of Nano-HA Content on the Mechanical Properties, Degradation and Biocompatible Behavior of Mg-Zn/HA Composite Prepared by Spark Plasma Sintering, *Mater. Character.*, 2019, **151**, p 620-631
34. S. Singh, R.M. Kumar, K.K. Kuntal, P. Gupta, S. Das, R. Jayaganthan, P. Roy, and D. Lahiri, Sol-Gel Derived Hydroxyapatite Coating on Mg-3Zn Alloy for Orthopedic Application, *J. Miner. Met. Mater. Soc.*, 2015, **67**, p 702-712
35. Z. Zhen, T.F. Xi, and Y.F. Zheng, A Review on In Vitro Corrosion Performance Test of Biodegradable Metallic Materials, *Trans. Nonferr. Met. Soc. China*, 2013, **23**, p 2283-2293
36. A. Purwar, R. Mukherjee, K. Ravikumar, S. Ariharan, and B. Basu, Development of ZrB2-SiC-Ti by Multi Stage Spark Plasma Sintering at 1600 °C, *J. Ceram. Soc. Jpn.*, 2016, **124**, p 393-402
37. S.S. Sib and J.W. Barlow, *Measurement and Prediction of Thermal Conductivity of Powdersat High Temperatures*, The University of Texas at Austin, Texas, 1994, p 321-329
38. H. Waizy, J.M. Seitz, J. Reifenrath, A. Weizbauer, F.W. Bach, A.M. Lindenberg, B. Denkena, and H. Windhagen, Biodegradable Magnesium Implants for Orthopedic Applications. *J. Mater. Sci*., 2013, **48**, p 39–50
39. D.R. Muthupandi, N. Viswanathan, S. Rameshbabu, and V. Kennedy, Plasma Electrolytic Oxidation and Characterization of Spark Plasma Sintered Magnesium/Hydroxyapatite Composites, *Mater. Sci. Forum*, 2013, **765**, p 827-831
40. R.M. Kumar, K.K. Kuntal, S. Singh, P. Gupta, B. Bhushan, P. Gopinath, and D. Lahiri, Electrophoretic Deposition of Hydroxyapaptite Coating on Mg-3Zn Alloy for Orthopedic Applicatin, *Surf. Coat. Technol.*, 2016, **287**, p 82-92
41. Z. Huan, C. Xu, B. Ma, J. Zhou, and J. Chang, Substantial Enhancement of Corrosion Resistance and Bioactivity of Magnesium by Incorporating Calcium Silicate Particles, *RSC Adv.*, 2016, **6**, p 47897-47906
42. L. Feller, Y. Jadwat, R.A. Khammissa, A.R. Meyerov, I. Schechter, and J. Lemmer, Cellular Responses Evoked by Different Surface Characteristics of Intraosseous Titanium Implants, *Biomed. Res. Int.*, 2015, **2015**, p 17194